APL Materials

RESEARCH ARTICLE | JUNE 26 2023

Vacuum deposited organic solar cells with BTIC-H as A–D–A non-fullerene acceptor

Special Collection: Advances in Organic Solar Cells

Irfan Habib ; Pascal Kaienburg ; Dondong Xia ; Olivia Gough ; Ming Zhu ; Joseph Spruce ; Weiwei Li ; Moritz Riede

APL Mater 11, 061128 (2023)
https://doi.org/10.1063/5.0148208

Vacuum deposited organic solar cells with BTIC-H as A–D–A non-fullerene acceptor

Cite as: APL Mater. 11, 061128 (2023); doi: 10.1063/5.0148208
Submitted: 28 February 2023 • Accepted: 25 May 2023 •
Published Online: 26 June 2023

Irfan Habib,[1,a)] Pascal Kaienburg,[1] Dondong Xia,[2] Olivia Gough,[1] Ming Zhu,[1] Joseph Spruce,[1] Weiwei Li,[3] and Moritz Riede[1,a)]

AFFILIATIONS

[1] Clarendon Laboratory, Department of Physics, University of Oxford, Oxford OX1 3PU, United Kingdom
[2] Institute of Applied Chemistry, Jiangxi Academy of Sciences, Nanchang 330096, People's Republic of China
[3] Beijing Advanced Innovation Center for Soft Matter Science and Engineering and State Key Laboratory of Organic-Inorganic Composites, Beijing University of Chemical Technology, Beijing 100029, People's Republic of China

Note: This paper is part of the Special Topic on Advances in Organic Solar Cells.
[a)] **Authors to whom correspondence should be addressed:** irfan.habib@physics.ox.ac.uk and moritz.riede@physics.ox.ac.uk

ABSTRACT

The record power conversion efficiency of solution-processed organic solar cells (OSCs) has almost doubled since non-fullerene acceptors (NFAs) replaced fullerene derivatives as the best-performing acceptor molecules. The successful transition from C_{60} to NFAs is still pending for vacuum-thermal evaporated (VTE) OSCs, not least because most NFAs are too large to be evaporated without breaking. Due to VTE's relevance in terms of industrial manufacturing, discovering high-performing VTE NFAs is a major opportunity for OSCs. Here, we fabricate evaporated OSCs based on the NFA BTIC-H known from solution processing. This A–D–A molecule has an unfused bithiophene core, 1,1-dicyanomethylene-3-indanone end groups, and hexyl side chains, making it small enough to be evaporated well. We pair BTIC-H with four commonly used evaporated donors—DCV5T-Me(3,3), DTDCPB, HB194, and SubNc—in planar heterojunctions. We observe appreciable photocurrents and a voltage loss of ~0.8 V, matching that of corresponding C_{60} devices. Donor:BTIC-H bulk heterojunctions likely face charge collection issues due to unfavorable microstructure. Our work demonstrates one of few NFA based evaporated OSCs with encouraging performance results and gives one potential starting point for molecule design of further NFAs suitable for VTE.

INTRODUCTION

For many years, fullerene derivatives were the best performing acceptor molecules for both vacuum thermal evaporation (VTE) and solution processing fabrication methods. Early non-fullerene acceptors, for example, perylene diimide dyes, achieved low lying energy levels but suffered from less favorable morphology and aggregation behavior.[1,2] In recent years, organic solar cells (OSCs) have shown a rapid advancement in power conversion efficiency (PCE), with the latest results fast approaching the 20% milestone.[3,4] This has been enabled by the development of novel electron-accepting molecules with an acceptor–donor–acceptor (A–D–A) structure with bulky side chains. These have largely replaced fullerene and fullerene derivatives as the acceptor molecule of choice in the active layers of OSCs.[1] This rapid advancement using these non-fullerene acceptors (NFAs) has been attributed to multiple reasons, with two key factors being the following: first, new A–D–A NFAs allow for far lower energy losses in the generation of free charges.[5,6] Second, these NFAs have significantly more absorption in the visible region—often extending into the near-infrared—compared to fullerene.[7]

To date, NFA molecules have largely been designed for solution processing and contain extended side chains, large molecular backbones, and an overall molecular weight >1000 g/mol. These properties often make them unsuitable for vacuum-based thermal evaporation (VTE) as bonds in these comparably large molecules break before they sublime. As a consequence of the current design paradigm, VTE OPV technology has not yet unlocked the advantages of NFAs. This represents a missed opportunity for the OPV field, as VTE has numerous advantageous properties, which include the following:[8]

- Equivalent devices show comparable efficiencies to fullerene-based solution processed devices.[9]
- It is an industry-proven manufacturing process used by the OLED industry.
- Small molecules have a well-defined molecular structure and weight, and purification via train sublimation is possible for molecules in VTE.
- Making complex multilayer stacks by sequential deposition is easy.
- It has precise control over layer thicknesses and film homogeneity.

There are few examples of VTE NFAs in recent years.[10] Noticeable examples include the phthalocyanine-based triple planar heterojunction a6T/SubPc/SubNc device, which was able to achieve a PCE of 8.4%.[11] More recently, devices made with the A–D–A molecule CBD as an acceptor and DTDCTB as a donor, achieved a PCE of ~0.86% and a low voltage loss of ~0.7 V.[12] Despite these promising results, there is little activity in the design of VTE compatible NFAs. In particular, A–D–A structures have brought great progress as donors for VTE and as acceptors for solution processing. Hence, NFAs need further exploration in the VTE field.

In this article, we investigate the molecule 2,2′-((2Z,2′Z)-((3,3′-dihexyl-[2,2′-bithiophene]-5, 5′-diyl)bis (methaneylylidene)) bis(3-oxo-2,3-dihydro-1H-indene-2,1-diylidene))dimalononitrile, named BTIC-H, an NFA with an unfused bithiophene core, 1,1-dicya nomethylene-3-indanone end groups, and hexyl side chains, for use in VTE OSCs by making planar heterojunction (PHJ) devices. DCV5T-Me(3,3), from here on referred to as DCV5T, DTDCPB, SubNc, and HB194 were chosen as electron donors for the active layer to cover a range of highest occupied molecular orbital (HOMO) and lowest unoccupied molecular orbital (LUMO) offset values in relation to BTIC-H's energy levels.

PHJs with DCV5T/BTIC-H showcased the best balance between simultaneously achieving a high V_{OC} of 0.96 V and a J_{SC} of 2.43 mA/cm^2 with a FF of 42%, resulting in values similar to the equivalent DCV5T/C_{60} PHJ using C_{60} as an acceptor. The DCV5T/BTIC-H PHJ performance also matches the voltage loss and PCE of solution-processed PCE12:BTIC-H bulk heterojunctions (BHJs) reported in the literature (~0.96 V).[13] The corresponding BHJ devices of DCV5T:BTIC-H performed poorly, highlighting the challenge for novel molecules of attaining a favorable morphology in BHJs.

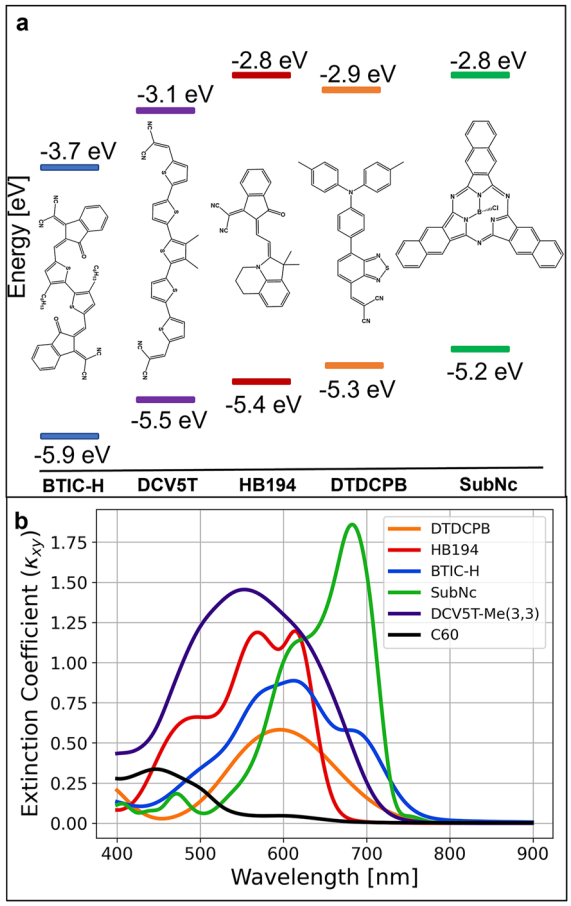

FIG. 1. (a) Chemical structures and energy levels of the molecules used in this study. HOMO levels were measured via ambient photoelectron spectroscopy (see Fig. S1 for details on fitting). LUMO levels were estimated using the empirical expression[14] *LUMO* = (*Optical Lumo*) · 1.14 + 1.19 eV that relates LUMO levels probed via IPES to the sum of the HOMO level and energy of absorption onset. The latter is determined from the extinction coefficients in (b). Extinction coefficients were calculated from the data obtained via spectroscopic ellipsometry using anisotropic models where relevant, with only the device relevant in-plane data shown, and with C_{60} data included as a reference.

RESULTS

The synthesis of BTIC-H is reported elsewhere,[13] and its molecular structure is shown in Fig. 1(a). BTIC-H has been used in a solution processed OSC with a polymer donor,[13] and its molecular structure makes it suitable for the VTE process as well. The donors shown in Fig. 1(a) were chosen because of their favorable energy level offsets, specifically their HOMO level offsets, which were measured using Ambient Photoelectron Spectroscopy (APS); see Fig. S1. The selection is motivated by the recent literature where HOMO offsets were shown to play a crucial role in charge generation for NFA OSCs.[5,15] Also shown are the in-plane extinction coefficients for each material [Fig. 1(b)]. BTIC-H shows absorption in a similar wavelength range as the evaporated donors used in this work. The absorption strength, indicated by the maximum of the extinction coefficient, is comparable to several of the donors. Compared to C_{60} as an acceptor, BTIC-H is shifted into the green and red absorption regions and has the potential to contribute significantly to the photocurrent. However, the extinction coefficient is lower than that of other A–D–A molecules, such as solution-processed NFAs,[7] or evaporated donors, such as DCV5T.

Current–voltage of PHJs

PHJ and BHJ devices were constructed in the following stack: ITO (110 nm)/MoO_3 (3 nm)/photovoltaic active layer (40 nm)/BPhen (8 nm)/Al (100 nm). In PHJs, the morphology of the active layer is much simpler than in the BHJ structure found in the best performing OSCs. This comes at the cost of decreased

photocurrents. For BHJ systems, the donor/acceptor interface is distributed throughout the volume of the blend, and the generation of free charge carriers can happen anywhere in this volume efficiently, whereas for PHJs, the volume from where photogenerated excitons are converted into free charge carriers is constrained to the interface (within the exciton diffusion length) between the donor/acceptor layers. In a PHJ, excitons generated far from the interface will generally recombine before they reach the D/A interface, where they would otherwise be split into free charge carriers. However, essential properties such as voltage losses and the charge generation process can be assessed in a PHJ before complicating the analysis with the BHJ morphology, of which the optimization is a major challenge for new molecules.

The stack used for the PHJ devices is shown in Fig. 2(a). All devices were made using a 20 nm nominal of the donor and a 20 nm nominal of the BTIC-H acceptor in the active layer. Current–voltage curves are shown in Fig. 2(b), with key performance metrics from the measurements summarized in Table I. The open circuit voltage (V_{OC}) for all PHJs, except SubNc, is between 0.94 and 0.96 V. SubNc devices show the lowest V_{OC} in the study with values around 0.78 V, which could be explained by the large HOMO offset between BTIC-H and SubNc. Photocurrents vary significantly between donors, with SubNc providing the highest measured short circuit current (J_{SC}) at 3.55 mA/cm^2. This is likely due to the high extinction coefficient of the material; therefore, more excitons are generated in the few nanometers that contribute to charge generation at the interface. HB194 PHJs showed the lowest J_{SC} at 0.4 mA/cm^2 despite having a stronger absorption than DTDCPB, which showed a J_{SC} of 1.16 mA/cm^2. DCV5T PHJs showed a J_{SC} of 2.43 mA/cm^2. Fill factors for all PHJs were less than 50%. HB194 PHJs showed a clear "S" shape and FF below 25%, which may indicate contact issues in the device,[16,17] which could also explain the low photocurrent despite the relatively high energetic offset between HB194 and BTIC-H. DCV5T and SubNc PHJs showed an FF value of ~42%, with DTDCPB PHJs showing a lower FF at 33%. We suspect that the dissociation of excitons into free charges is not 100% efficient for all tested donors. The moderate FF, lower than what one might expect for PHJ devices,[10] could indicate field-assisted charge generation. Since the electric field in a solar cell is higher at J_{SC} than at the maximum power point, a charge generation process that depends on the electric field, and, thus, the applied voltage, would restrict the FF.

When used as acceptor in solution-processed devices with the high-performance polymer PCE12 as a donor,[13] optimized devices achieved a lower V_{OC} of 0.69 V, a J_{SC} of 2.68 mA/cm^2, an FF of 52%, and an overall PCE of 0.96%. The polymer:BTIC-H device showcased a higher FF than the devices investigated in this study. Our best evaporated devices using DCV5T and SubNc as donors achieved comparable or higher J_{SC} and PCE values and showcased higher V_{OC} compared to the PCE12 devices. The HOMO of PCE12 measured by using a UPS is shown in the literature to be −4.9 eV,[18] which is much higher lying than the donors used in this study [see Fig. 1(a)].

Next, we put the obtained performance in context with the energy levels shown in Fig. 1. Optical transfer matrix method (TMM) simulations were also carried out to better understand the obtained J_{SC} and link it to the molecular energy levels. By normalizing the J_{SC} by the simulated maximum J_{SC}, which assumes 100% internal quantum efficiency (IQE), i.e., that every photon absorbed within the given region of the interface results in an extracted charge pair, we can account for different donor absorptions and, thus, get an estimate of the integrated IQE for the studied systems. This allows us to assess the impact of the energetic offsets on charge generation efficiency (assuming collection is the same for

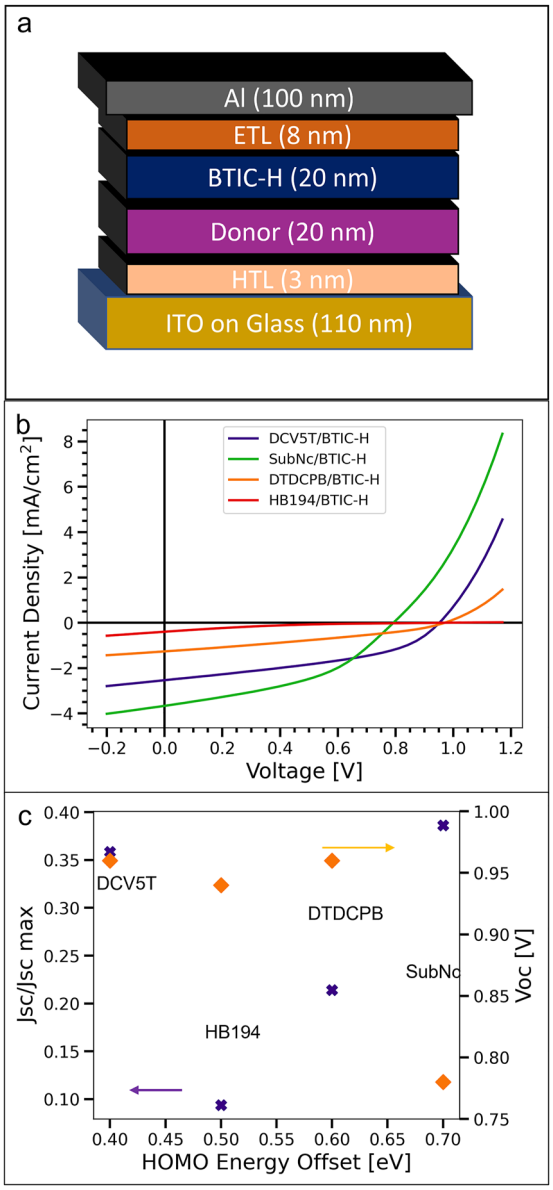

FIG. 2. (a) Device stack for PHJ devices. BPhen was used as the ETL, and MoO_3 was used as the HTL; nominal thicknesses were ITO (110 nm)/MoO3 (3 nm)/donor (20 nm)/BTIC-H (20 nm)/BPhen (8 nm)/Al (100 nm). (b) JV measurements under illumination of individual PHJs using donors DCV5T, SubNc, DTDCPB, and HB194. (c) Plot showing the effect of the HOMO energy offset between donors and BTIC-H on the ratio between the J_{SC} to the simulated J_{SC} assuming 100% IQE, and the V_{OC}. The purple crosses indicate the J_{SC}/J_{SC}-max ratio, and the diamonds indicate the V_{OC}. The donor molecules the offsets refer to are listed on the image.

TABLE I. Mean key metrics from JV measurements of donor/BTIC-H devices shown in Fig. 2(b). The voltage loss is calculated via $\Delta V = \frac{E_g}{q} - V_{OC}$, where E_g is calculated from the inflection point of the EQE. The uncertainties indicated are given by the statistical errors in the data, with sample sizes around 10–11 devices each. Equivalent AM1.5G spectra intensities are shown for the measurements, and mismatch corrected J_{SC} values are also shown for a scaled equivalent 100 mW/cm^2 AM1.5G spectra.

	DCV5T	DTDCPB	HB194	SubNc
V_{OC} (V)	0.96 ± 0.01	0.96 ± 0.01	0.94 ± 0.01	0.78 ± 0.01
FF (%)	41.9 ± 0.3	33.2 ± 0.2	13.4 ± 0.1	42.5 ± 0.2
$J_{SC\ measured}$ (mA/cm^2)	2.43 ± 0.10	1.16 ± 0.05	0.4 ± 0.04	3.55 ± 0.05
Equivalent intensity (AM1.5G)	0.95	0.96	0.94	1.01
$J_{SC\ corrected}$ (mA/cm^2)	2.55 ± 0.11	1.25 ± 0.05	0.43 ± 0.04	3.51 ± 0.05
PCE (%)	1.02 ± 0.04	0.40 ± 0.01	0.05 ± 0.01	1.20 ± 0.03
Voltage loss (V)	0.81 ± 0.02	0.80 ± 0.02	0.95 ± 0.02	0.92 ± 0.02

all devices, which should be the case for PHJs). Simulated maximum J_{SC} contributions are shown in Fig. S2(a). Further details about using the maximum J_{SC} can be found in the discussion around Fig. S2 in the supplementary material. The relationship between HOMO offset and V_{OC} in Fig. 2(c) shows that the V_{OC} decreases with increasing offset, an expected result considering the established relation between donor HOMO and acceptor LUMO and V_{OC}.[19] Regarding the J_{SC}, we note that all HOMO and (estimated) LUMO offsets are larger than 0.4 eV, which is thought to facilitate efficient charge generation for solution-processed NFAs,[5,15] which is not the case in our dataset based on BTIC-H. From a pure energy level perspective, larger offsets should yield more efficient charge generation up to a certain point where the Marcus inverted regime is entered and charge generation efficiency decreases again.[20] Accounting for the difference in absorption, Fig. 2(c) shows that the efficiency of free charge generation decreases with larger offsets. The exact reasons for this are still under investigation. Possible reasons are that the energetic landscape at the buried interface itself might be very different from the energy levels probed during APS measurements, that we enter the Marcus-inverted regime,[20] or that factors other than energetics governing the charge transfer processes occurring when transitioning from a bound to an unbound state.

It should be noted that in a PHJ device, only a certain volume surrounding the interface will normally contribute to the charge generation in the device. The total size of this region is governed by the materials exciton diffusion length. SubNc, it should be further noted, has been shown in the literature to generate charges efficiently in a neat film,[21] which will inflate its J_{SC} relative to other devices.

Comprehensively determining the exciton diffusion length for all the materials used in this study is out of the scope of this paper; however, values from the literature were used for SubNc (20 nm),[22] which is remarkably large, and DCV5T (10 nm).[23] When no value could be found, 10 nm was assumed.

Voltage loss for PHJs

The external quantum efficiency (EQE) of the PHJs was measured with a high dynamic range over up to five orders of magnitude and is shown in Fig. 3(a). EQEs are relatively low, with values and trends matching the measured J_{SC} reported above. Figure 3(b) shows the EQE on the log scale, and no clear shoulder is visible in most of the tails of the EQE, with the exception of HB194, implying that the CT state is either quite close to the singlet or that its absorption and oscillator strength are very weak.

Voltage loss analysis was carried out following the detailed balance principle as suggested in the literature,[24–26] and the photovoltaic gap of each device was taken to be the inflection point of the EQE. Due to SubNc devices displaying a slowly decaying tail below 1.5 eV, which cannot be fully resolved with our setup, we refrain from applying the voltage loss analysis to this system, with Fig. S3 showing the fit results. The results of the analysis are shown in Figs. 3(c) and 3(d). Breaking down the voltage loss yields the following equation:

$$\Delta V = \Delta V_{SQ} + \Delta V_{J_{SC}} + \Delta V_{rad} + \Delta V_{nonrad} = \frac{E_g}{q} - V_{OC},$$

where q is the elementary charge of an electron and E_g is the photovoltaic gap estimated from the inflection point of the EQE. $\Delta V_{J_{SC}}$ is a result of the J_{SC} being lower than the maximum J_{SC} obtained from an ideal semiconductor with the same photovoltaic gap (E_g) and follows the J_{SC} shown in Fig. 2(b), with highest losses in HB194/BTIC-H (0.09 V) and lowest losses in DCV5T/BTIC-H (0.05 V), with DTDCPB/BTIC-H showing a loss of 0.08 V. ΔV_{rad} represents the losses arising from radiative recombination from sub-gap states, commonly attributed to be CT states.[25] DTDCPB/BTIC-H and HB194/BTIC-H show the highest ΔV_{rad} (0.16 and 0.11 V, respectively), while DCV5T PHJs show the lowest (0.08 V). DCV5T devices show steeper tails in the EQE than DTDCPB or HB194 devices, which explains the lower ΔV_{rad}. HB194 PHJs show a broad shoulder in the EQE, which gives rise to the large ΔV_{rad} observed. The ΔV_{nonrad} is highest in HB194 devices (0.45 V), followed by DCV5T/BTIC-H (0.40 V) and DTDCPB devices showing the lowest values (0.29 V). Total voltage losses for these PHJs are summarized in Table I, and individual losses are shown in Table S2. DCV5T/BTIC-H and DTDCPB/BTIC-H show relatively low total voltage losses (0.81 and 0.80 V), far lower than what was achieved with solution-processed devices using BTIC-H (~0.96 V).[13]

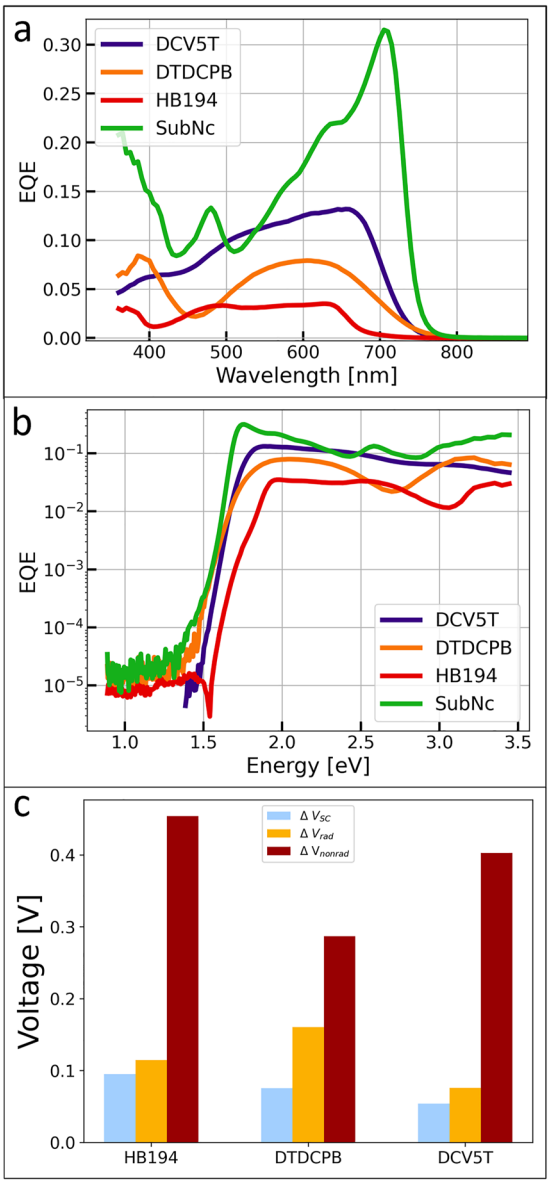

FIG. 3. (a) External Quantum Efficiency (EQE) measurements of PHJ devices shown in Fig. 2, plotted on a linear scale. (b) The same EQE as in (a), plotted on a logarithmic scale. No shoulders are discernible in the EQE, except for the HB194 PHJ at ~1.7 eV. (c) Voltage loss breakdown showing the $\Delta V_{J_{SC}}$, ΔV_{rad}, and ΔV_{nonrad} contributions. Fitting details can be found in Fig. S3. SubNc was omitted from the voltage loss breakdown due to the gradual decay in its EQE tail, which could not be fully resolved with our setup. Fitting the SubNc EQE as a result would, therefore, be misleading.

BTIC-H vs C_{60}

Given the combination of relatively good J_{SC} and low voltage losses, the BTIC-H DCV5T system was further explored. BHJ devices were made, and the active layers used in these devices used the same nominal thickness as the PHJs, i.e., 40 nm in a 1:1 volumetric ratio. The effect of the same thickness in the active layer between PHJ and BHJ devices is that the absorptance is roughly similar between the two when neglecting changes in the interference pattern. JV and EQE results are shown in Figs. 4(a), 4(b), and 4(d) with key metrics summarized in Table II. DCV5T:BTIC-H BHJs showed a V_{OC} of 0.93 V, a J_{SC} of 0.53 mA/cm^2, and a FF of 24.6%.

The increased interface in a BHJ should ideally result in an increase in short-circuit current because more excitons reach the exciton-splitting interface. However, this is not observed for the DCV5T:BTIC-H BHJs. Two possible reasons for this are as follows: (1) The generation of free charges is impeded compared to the PHJ, e.g., by an energetic barrier that is introduced through orientation[27,28] or aggregation changes in the molecules upon mixing, or (2) there is an issue with charge collection in the BHJ devices. Both could also explain the lower FF of ~26% shown in the BHJ JV curves as opposed to the ~42% exhibited in the PHJ JV. It is important to note that the V_{OC} has only slightly dropped, from 0.96 V in the PHJ to 0.93 V in the BHJ. This makes an energetic barrier less likely as the primary loss mechanism to explain the low photocurrent in the BHJ devices. If, on the other hand, charge collection is causing a lower FF, this would be mediated by a lower mobility and/or an increase in recombination in the BHJs. OTRACE measurements[29] probe the faster mobility species and confirm a very low value in the DCV5T:BTIC-H BHJs of 1.3×10^{-6} cm^2/V s (see Fig. S4). The likely reason for low mobility is an unfavorable microstructure, which we examine later on.

Equivalent C_{60} reference devices where the BTIC-H is replaced with C_{60} as an acceptor were also made and measured. DCV5T/C60 PHJs showcased a V_{OC} value of 0.99 V, a J_{SC} of 3.93 mA/cm^2, and a FF of 45%. DCV5T/C60 PHJs showed a better performance across all key metrics than equivalent BTIC-H PHJs, most noticeably in the J_{SC} despite absorbing fewer photons. In the C_{60} BHJs, the increase in interface area results in a substantially higher J_{SC} of 8.2 mA/cm^2, more than double that observed for a PHJ of the same thickness, a slightly smaller V_{OC} of 0.93 V, and a lower FF of 41%. The J_{SC} is further increased in the thicker 60 nm device (Fig. S4), which is not at all observed in the BTIC-H BHJs. The FF does reduce upon increasing the thickness of the active layer in the C_{60} reference BHJs, which may be caused by higher charge collection losses at greater thicknesses, but the higher J_{SC} observed still contributes to a higher PCE in the thicker films. It should be noted that in optimized devices, DCV5T:C_{60} BHJs are reported to show similar V_{OC} values (~0.96 V), albeit with much higher J_{SC} (~13 mA/cm^2) and better FF (~60%).[30] This highlights the impact optimization can have on the photocurrents of OSCs but also shows that the value of V_{OC} is mostly impacted by the choice of materials rather than the processing conditions.

Figure 4(c) shows the voltage loss breakdown between C_{60} and BTIC-H devices in combination with DCV5T. Fitting details for the extrapolation of the EQE can be found in Fig. S5. $\Delta V_{J_{SC}}$ for C_{60} devices are lower compared to the BTIC-H devices, reflecting the reduction in J_{SC} seen in the JV. For the C_{60} PHJ devices, ΔV_{rad}, is lower than the BTIC-H PHJ. Interestingly, despite showing far better overall performance than BTIC-H devices, the C_{60} BHJs show much higher ΔV_{rad}. This is likely due to the fact that the BTIC-H BHJ devices show much lower photocurrents, close to an order of magnitude difference. This makes a fair comparison

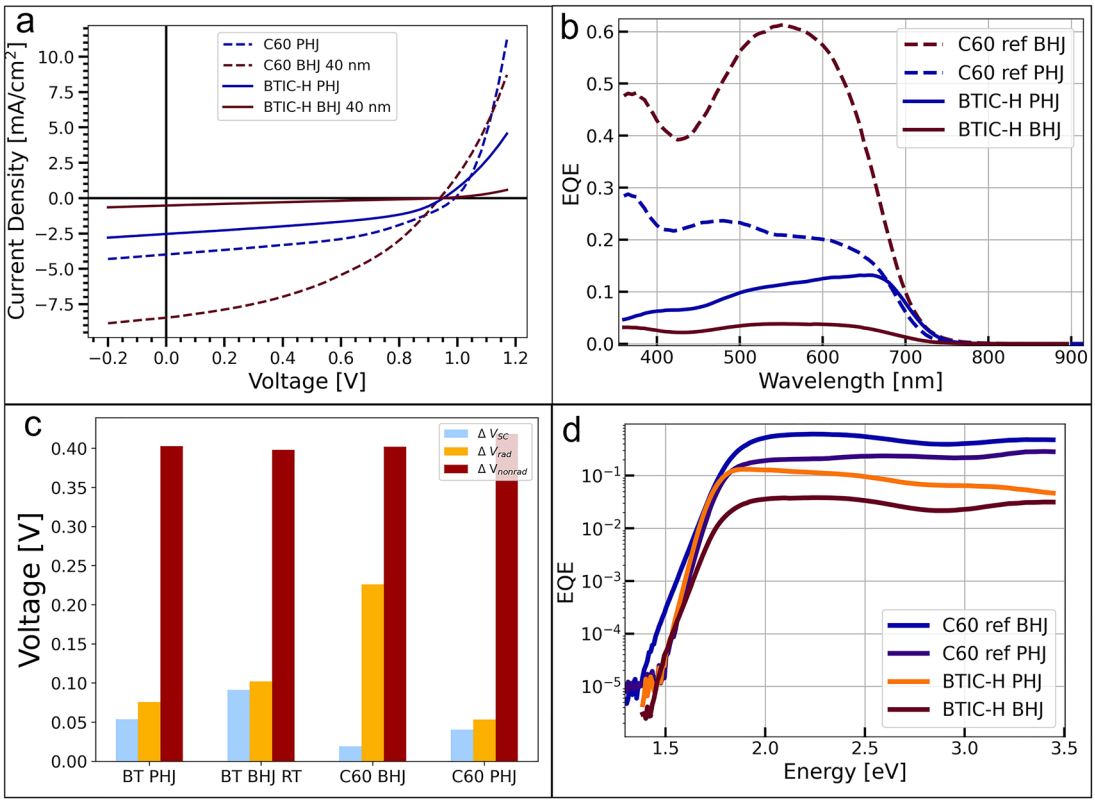

FIG. 4. (a) JV results under illumination of BTIC-H PHJ and BHJ devices and their C_{60} counterparts. PHJ devices are identical to those shown earlier in Fig. 3, and BHJ devices have a 1:1 vol. blend of the acceptor and donor, with a total thickness of 40 nm. (b) EQE results of the same devices in (a). (c) Voltage loss breakdown according to the detailed balance principle showing $\Delta V_{J_{SC}}$, ΔV_{rad}, and ΔV_{nonrad} contributions. (d) EQE of the same devices, plotted on a logarithmic scale. Fitting details are shown in Fig. S3.

between the BTIC-H BHJ and the C_{60} BHJ devices difficult and should be avoided. Both BTIC-H and C_{60} devices show similar ΔV_{nonrad}. Total voltage losses are displayed in Table II, showing similar voltage losses across both BTIC-H and C_{60} PHJs—0.81 and 0.79, respectively—with values within error margins of each other. Despite performing poorly compared to C_{60} BHJs, BTIC-H BHJs show lower voltage losses, 0.87 vs 0.93 V. Individual losses are shown in Table S3.

TABLE II. Mean key metrics from JV measurements in Fig. 2(b), including open circuit voltage (V_{OC}), fill factor (FF), short circuit current (J_{SC}), power conversion efficiency (PCE), and total voltage loss calculated from the EQE using $V_{loss} = \frac{E_g}{q} - V_{OC}$, where E_g is calculated from the inflection point of the EQE. The uncertainties indicated are given by the statistical errors in the data, with sample sizes of 10–11 devices each. Equivalent AM1.5G spectra intensities are shown for the measurements, and mismatch-corrected J_{SC} values are also shown for a scaled equivalent of 100 mW/cm^2 AM1.5G spectra. More results for thickness variations and heated substrate devices are shown in Table S3.

	DCV5T/BTIC-H PHJ	DCV5T:BTIC-H BHJ	DCV5T/C_{60} PHJ	DCV5T:C_{60} BHJ
V_{OC} (V)	0.96 ± 0.01	0.93 ± 0.01	0.99 ± 0.0	0.93 ± 0.0
$J_{SC\ measured}$ (mA/cm^2)	2.43 ± 0.10	0.53 ± 0.01	3.93 ± 0.19	8.20 ± 0.35
Equivalent intensity (AM1.5G)	0.95	0.95	0.94	0.94
$J_{SC\ corrected}$ (mA/cm^2)	2.55 ± 0.11	0.57 ± 0.01	4.20 ± 0.20	8.77 ± 0.37
FF (%)	41.9 ± 0.3	24.6 ± 0.1	45.2 ± 0.5	41.2 ± 0.6
PCE (%)	1.02 ± 0.04	0.13 ± 0.01	1.75 ± 0.1	3.09 ± 0.12
Voltage loss (V)	0.81 ± 0.2	0.87 ± 0.2	0.79 ± 0.2	0.93 ± 0.2

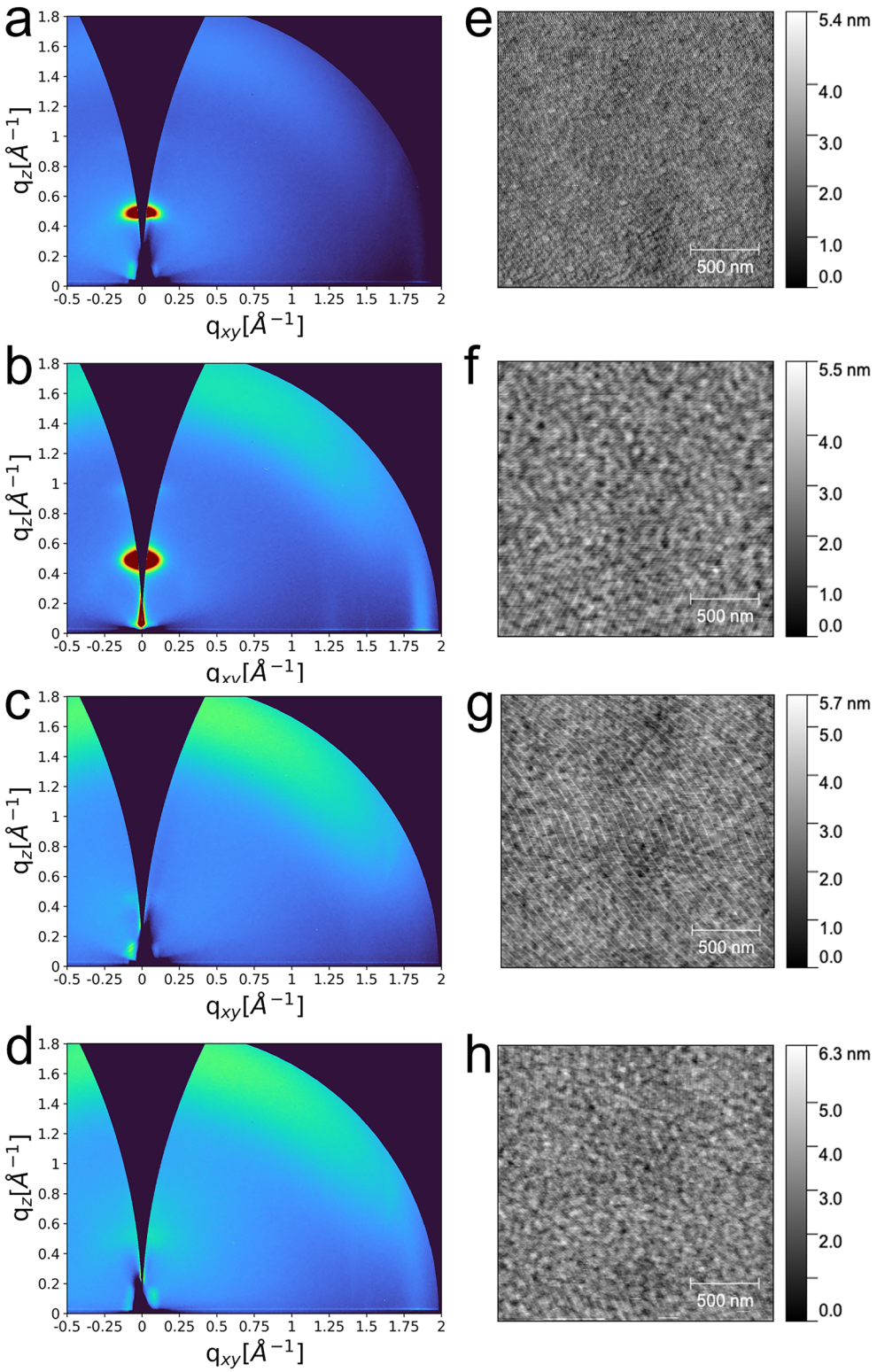

FIG. 5. GIWAXS images of 20 nm films of BTIC-H (a) and (b) deposited on glass substrates held at room temperature (a) and 80 °C (b), and BTIC-H:DCV5T (1:1 by vol., 40 nm) blends (c) and (d) deposited on glass substrates held at room temperature (c) and 80 °C (d). AFM images on identical samples are shown alongside (e)–(h).

Microstructure of the active layer

To further investigate the poor performance of OSCs based on BTIC-H:DCV5T, the photovoltaic active layers were studied using AFM and GIWAXS. Figure 5 shows GIWAXS images alongside AFM images of identical samples of neat BTIC-H films and DCV5T:BTIC-H blends deposited on substrates held at room temperature (RT) and 80° C (HT). Similar images of DCV5T are shown in Fig. S7. No clear scattering is observable for DCV5T at room temperature (Fig. S7); however, there is a strong Bragg peak present at ~0.5 $Å^{-1}$ for the BTIC-H neat film in the out of plane direction [Fig. 5(a)], indicative of lamellar stacking of the BTIC-H molecules, and has been attributed to the dihedral angle in the bithiophene core of the molecule caused by the hexyl side chains.[13] These peaks disappear upon blending [Fig. 5(c)], indicating a significant disruption of the stacking order present in the neat film. This could be caused by a strong degree of intermixing between the molecules, which create larger amorphous mixed phase regions within the layer. Alternatively, the new blend morphology may still retain large acceptor-rich domains like those in the neat film, but these domains might now be amorphous due to interactions with the DCV5T molecules. Since a good FF and efficient collection of charges in a BHJ require the right degree of phase separation, we believe the former case to be present here.

When observing the HT BTIC-H sample, a Bragg peak of ~1.8 $Å^{-1}$ appears in-plane [Fig. 5(b)], indicating pi–pi stacking in a plane parallel to the substrate, and upon blending, the HT sample shows more pronounced ordering than the RT blend, yet is still weak compared to the neat BTIC-H images. Nonetheless, in the blend films, it is still instructive to note the improvement in crystallinity with heating, as shown by the intensifying out-of-plane peak at ~0.5 $Å^{-1}$ indicative of stronger lamellar stacking of the BTIC-H molecules, and the increase in pi–pi stacking with an intensifying in-plane feature at ~1.8 $Å^{-1}$. Following our earlier reasoning that this crystallinity is tracking, to some extent, the mixing in the blends, it stands to reason that the HT blend samples show less mixing, i.e., phase segregation increases upon depositing the film on a heated substrate. This is a phenomenon that has been observed for similar systems in the literature.[31] AFM images are shown alongside GIWAXS for comparison, where an increase in aggregation in the films upon heating is apparent. Furthermore, in the blend films, the root mean squared (rms) roughness increases with heating. This supports the idea from the GIWAXS that heating leads to a stronger crystalline structure, with the RT blend, in particular, having high levels of intermixing. If a film is highly amorphous, it is likely to be smoother, and vice versa, as the film becomes more crystalline, the surface can become less smooth. The rms roughness of the RT blend [Fig. 5(g)] is 667 ± 45 pm, and the rms roughness of the HT blend [Fig. 5(h)] is 820 ± 65 pm. Full OSC devices were made to assess the impact of this heating-induced change in morphology on the photocurrent, and while minor gains were observed, they did little to bridge the stark gap in photocurrents between C60 and BTIC-H BHJs. The results for these devices are also shown in Table S3, with JV measurements shown in Fig. S4.

It is worth highlighting here that critical device properties, such as photocurrents and open circuit voltages, can be probed in PHJ architectures, which are easily made with VTE, and thereby avoid issues related to the miscibility of donor and acceptor molecules and the need to obtain the right degree of phase separation in a BHJ. By deconvoluting properties related to the energetics at the donor/acceptor interface and microstructure effects, this screening protocol allows engineering molecular properties in a more step-by-step manner, raising hopes for more rational design and quicker progress. In follow-up work, shortening sidechains and improving material purity are expected to improve performance. The general targets of evaporated NFAs include achieving efficient charge generation even at low electric fields while maintaining low voltage loss. This is facilitated by the right interface energetics[5,15] and properly tuned molecular stacking. Furthermore, favorable miscibility is needed for efficient charge collection in the BHJ and absorption further into the infrared is desirable. For all this, the backbone, end groups, and short sidechains need to be optimized without exceeding molecular weight restrictions and avoiding weak bonds where possible. Once these challenges are mastered and evaporable NFAs have enabled efficiency increases, the real-world impact of VTE OSCs is imminent due to the advanced industrial production technology of evaporated organic semiconductors.

CONCLUSION

We the report encouraging performance of evaporated organic solar cells using the non-fullerene acceptor BTIC-H, originally developed for solution processing. The low molecular weight and relatively simple molecular structure of BTIC-H, giving it an advantage over many NFAs in terms of synthetic complexity, make it feasible for evaporation. Despite the molecule not being optimized for evaporation, we achieve a high open-circuit voltage of 0.96 V and a decent short circuit current of 2.43 mA/cm^2 when used with DCV5T as a donor in a planar heterojunction device. Furthermore, a voltage loss of 0.81 V, comparable to equivalent fullerene devices (0.79 V), was achieved for the DCV5T planar heterojunctions. Bulk heterojunctions of DCV5T:BTIC-H showed similar open circuit voltages (0.93 V) but poor short circuit currents (0.53 mA/cm^2), which was likely due to the poor morphology of the blend layer inhibiting efficient charge collection.

By using a combination of PHJ and BHJ structures to investigate BTIC-H as a VTE compatible NFA, we were able to study D/A interface energetics and their effect on photocurrent generation and voltage loss separately from morphological effects in mixed blends. This screening procedure helps to identify suitable donors and was enabled by the ease of sequential deposition in VTE. While these results are certainly encouraging, attaining a higher PCE and doing better on the trade-offs encountered in this work is key to the success of evaporable NFAs, which, once identified, hold great promise for commercial OSC applications in the near future.

METHODS

Materials and substrates

ITO (20 Ω/sq on Eagle XG glass, rms roughness <7 Å) was purchased from Thin Film Devices (TFD) Inc., USA. C_{60} was purchased from Creaphys GmbH, Germany, in its optoelectronic grade (sublimed multiple times). SubNc, DTDCPB, HB194, and BPhen were purchased in a sublimed grade from Luminescence Technology Corp., as well as MoO_3. DCV5T-Me(3,3) was purchased from Synthon Chemicals GmbH and Co. KG, Germany. BTIC-H was synthesized as detailed in Ref. 13.

Sample fabrication

Prior to deposition, all substrates were cleaned for 10 min in an ultrasonic bath of 2.5% Hellmanex solution, followed by DI water, acetone, and isopropanol. The substrates were treated with O_2 plasma for 10 min before being loaded into the vacuum chamber. All layers were thermally evaporated in a vacuum chamber (EVAP300, Creaphys, base pressure 10^{-7} mbar), followed by transfer into an N_2-filled glovebox without vacuum break for encapsulation. Layers with a nominal thickness determined from tooled Quartz Crystal Microbalances (QCMs) were MoO_3 (3 nm, 0.1 Å/s), donor:acceptor (1:1 vol., 0.2 Å/s total rate) for BHJs, 0.1 Å/s for BTIC-H and DCV5T neat layers, 0.2 Å/s for other donors, BPhen (8 nm, 0.1 Å/s), and Al (~100 nm, 1 Å/s). The solar cells had an active area of 0.08 cm^2 defined by the geometric overlap between ITO and Al, and there were eight solar cells per substrate. Samples for spectroscopic ellipsometry (SE) were evaporated on glass for all samples, and additionally on Si with native oxide, and Si with 150 nm thermal oxide substrates for BTIC-H, HB194, DTDCPB, and DCV5T. APS samples were made on ITO on glass and were all between 20 and 40 nm, with the exception of HB194, which was 10 nm deposited on Au. APS and SE samples for HB194 and DTDCPB, as shown in the article, were made at the EPSRC National Thin Film Cluster Facility (NTCF) for Advanced Functional Materials. GIWAXS and AFM samples were identical and deposited on glass.

Spectroscopic ellipsometry

SE was carried out using a Woollam RC2 spectroscopic ellipsometer at 50°, 55°, 60°, 65°, 70°, and 75° angles of incidence. Single-component films on glass were prepared in a similar fashion to the devices. The acquired ψ and Δ spectra were model-fitted with the CompleteEASE software from J.A. Woollam Company to obtain the optical constants n and κ. Using B spline models, anisotropic fits were performed yielding in-plane and out-of-plane components and the results were confirmed by matching transmission data.

JV

Current density–voltage characteristics were measured under illumination from a Newport Oriel Sol3A solar simulator with a Xe arc lamp. Mismatch correction was applied to the data according to Ref. 32 and the equivalent AM1.5G intensities provided with the measured results.

EQE

Sensitive external quantum efficiency (EQE) measurements were performed using a custom-built setup. White light from a tungsten-halogen light source (Princeton Instruments, TS-428, 250 W) was diffracted by wavelength using a monochromator (Princeton Instruments, Spectra-Pro HRS300, Triple Grating Imaging Spectrograph). Using spectral filters (Thorlabs, edge pass and long pass filters), stray light and higher-order diffractions were removed. The light was modulated using a chopper wheel (Stanford Research Systems, SR450, Optical Chopper) before being focused onto the device under testing. The resulting photocurrent was pre-amplified (Zürich Instruments, HF2TA Current Amplifier) before being read out by a lock-in amplifier (Zürich Instruments, HF2LI Lock-In Amplifier). Data were measured and analyzed with software, which can be accessed on GitHub: https://github.com/AFMD/sEQE-Setup

OTRACE

Open-circuit corrected charge carrier extraction was performed with a PAIOS system from Fluxim AG, Switzerland. The 60 nm-thick BHJ samples were illuminated with a white LED light for 100 μs until a steady-state V_{oc} was reached. Delay times were varied between a few μs and 1 ms. The linear voltage pulse (ramp rate of 200 and 400 V/ms) was chosen long enough (~30 μs) such that all mobile carriers were extracted, and the current peak decayed to the displacement current obtained from a dark measurement with no offset voltage applied. The analysis follows Eq. (24) in Ref. 33.

Transfer matrix method

TMM optical simulations to calculate the short-circuit current density in the case of complete carrier collection (100% IQE) were performed with the published code.[17] A stack of glass, 110 nm of ITO, 3 nm of MoO_3, a varied thickness of donor:C_{60}, 8 nm of BPhen, and 100 nm of Al were used with a normal incidence of AM1.5G illumination. The complex refractive index $\tilde{n} = n + i\kappa$ of all materials, except Al, in the study were measured in-house with ellipsometry as described above, including the DCV5T:BTIC-H blend. The $\tilde{n}$ of Al was taken from Ref. 34.

Voltage loss calculation

We follow the detailed balance analysis by Rau *et al.*[24] The optical bandgap E_g was defined as the inflection point of the EQE absorption edge[24] on a linear scale. Detailed balance theory[35] yields V_{oc}^{SQ} and J_{sc}^{SQ}. The losses from imperfect photocurrent were calculated as $\Delta V_{SC} = k_B T/q \cdot \ln\left(J_{sc}^{SQ}/J_{sc}\right)$. The radiative V_{oc}^{rad} was calculated assuming reciprocity between EQE and electroluminescence[36,37] via $V_{oc}^{rad} = k_B T/q \cdot \ln\left(\int_{E_{min}}^{\infty} EQE \cdot \phi_{AM1.5g} dE / \int_{E_{min}}^{\infty} EQE \cdot \phi_{bb} dE\right)$. Here, ϕ_{bb} is the black-body spectrum and E_{min} was chosen small enough such that $V_{oc}^{rad}(E_{min})$ saturates as discussed in Fig. S3. The remaining loss terms were then calculated via $\Delta V_{SQ} = E_g - V_{oc}^{SQ}$, $\Delta V_{rad} = V_{oc}^{SQ} - \Delta V_{SC} - V_{oc}^{rad}$, and $\Delta V_{nonrad} = V_{oc}^{rad} - V_{oc}$.

GIWAXS

Grazing Incidence Wide Angle X-ray Scattering (GIWAXS) scans were taken at XMaS: The UK Materials Science Facility (BM28) at the European Synchrotron Radiation Facility (ESRF; experimental session 28-01-1306). A MAR detector was used to acquire data at 10 KeV.

AFM

Atomic force microscopy was performed in tapping mode over 256 lines using the Asylum Research MFP-3D AFM (Oxford Instruments) with HQ-150-Au model cantilever tips. Analysis of the AFM was performed with the free software Gwyddion. Roughness values were evaluated as the root mean squared height of the image area. Scans were done in three separate places on the film, and error

was assigned as the standard deviation between rms roughnesses of the scan areas. Please note the comb-like artifact on the scans, due to a filtering fault on the microscope, resulting in a 50 Hz "click." The amplitude of the click is of a similar order of magnitude to the features of the film, meaning that the artifact is particularly visible. In this case, it is not possible to use Fourier notch filtering on the 2D image because the random distribution of phases across all the many horizontal scan lines in the image averages this component to around zero. The presence of these artifacts does not change the analysis.

APS

Ambient photoelectron spectroscopy spectra were measured using an *Ambient-pressure Photoemission Spectroscopy system* (*KP TECHNOLOGY, APS02*). HOMO levels were measured via UV light (−4.0 to −7 eV) illuminating the samples to generate photoemission of electrons. The photoemitted electrons interact with air molecules and generate radicals. These radicals are then collected by a positively biased tip. The HOMO levels were determined by fitting a straight line from the cube root photoemission intensity to the baseline. The analysis follows the process used in Ref. 28.

SUPPLEMENTARY MATERIAL

Additional details about the study, including the details about the APS and EQE fits, a discussion about the simulated maximum short-circuit current, OTRACE measurements, and additional JV and GIWAXS measurements can be found in the supplementary material.

ACKNOWLEDGMENTS

GIWAXS images were taken at XMaS: The UK Materials Science Facility (BM28) at the European Synchrotron Radiation Facility (ESRF; experimental session 28-01-1306). We are grateful to all the beamline team staff for their support, in particular Oier Bikondoa. We acknowledge the EPSRC National Thin Film Cluster Facility (NTCF) for Advanced Functional Materials, hosted by the Department of Physics at the University of Oxford, where some of the samples were prepared, and thank Dr. Jin Yao, the facility manager, for his support, as well as Zhenlong Li. The authors would also like to thank David Sharp for his assistance with AFM measurements. The NTCF was funded by ESPRC (Grant No. EP/M022900/1), the Wolfson Foundation, and the University of Oxford. I.H. would like to acknowledge the Oppenheimer Memorial Trust and the Firstrand Foundation for funding. P.K. acknowledges EPSRC for funding of a Postdoctoral Fellowship Grant No. EP/V035770/1. O.G. acknowledges the funding from the Wolfson-Marriott Graduate Scholarship from Wolfson College, Oxford.

AUTHOR DECLARATIONS

Conflict of Interest

Author Contributions

The original draft of the paper was written by I.H. with contributions by P.K. All authors contributed to reviewing and editing the work. D.X. synthesized the BTIC-H material. I.H. made and measured the samples and led the data analysis. M.Z., I.H., and J.S. measured and analyzed the APS data, and M.Z. made some of the APS samples. I.H. measured and analyzed the ellipsometry data. O.G. measured and analyzed the AFM data. I.H. and O.G. measured GIWAXS images and I.H. analyzed the resulting GIWAXS data. I.H. and P.K. did the voltage loss analysis. W.L., M.R., and I.H. conceptualized the study, and W.L. and M.R. supervised the project.

Irfan Habib: Conceptualization (equal); Formal analysis (lead); Investigation (lead); Visualization (lead); Writing – original draft (lead); Writing – review & editing (equal). **Pascal Kaienburg**: Conceptualization (supporting); Data curation (supporting); Formal analysis (supporting); Visualization (supporting); Writing – original draft (supporting); Writing – review & editing (equal). **Dondong Xia**: Investigation (equal); Writing – review & editing (equal). **Olivia Gough**: Formal analysis (supporting); Investigation (supporting); Writing – review & editing (equal). **Ming Zhu**: Formal analysis (supporting); Investigation (supporting); Writing – review & editing (equal). **Joseph Spruce**: Formal analysis (supporting); Investigation (supporting); Writing – review & editing (supporting). **Weiwei Li**: Conceptualization (equal); Supervision (equal); Writing – review & editing (equal). **Moritz Riede**: Conceptualization (equal); Supervision (equal); Writing – review & editing (equal).

DATA AVAILABILITY

The data that support the findings of this study, including the cluster recipes for making the APS and SE samples for DTDCPB and HB194, are available from the corresponding author upon reasonable request.

REFERENCES

[1] A. Armin *et al.*, "A history and perspective of non-fullerene electron acceptors for organic solar cells," Adv. Energy Mater. **11**(15), 2003570 (2021).
[2] C. Yan *et al.*, "Non-fullerene acceptors for organic solar cells," Nat. Rev. Mater. **3**(3), 18003 (2018).
[3] L. Zhu *et al.*, "Single-junction organic solar cells with over 19% efficiency enabled by a refined double-fibril network morphology," Nat. Mater. **21**(6), 656–663 (2022).
[4] Y. Li *et al.*, "Recent progress in organic solar cells: A review on materials from acceptor to donor," Molecules **27**(6), 1800 (2022).
[5] S. Karuthedath *et al.*, "Intrinsic efficiency limits in low-bandgap non-fullerene acceptor organic solar cells," Nat. Mater. **20**(3), 378–384 (2021).
[6] S. Chen *et al.*, "Efficient nonfullerene organic solar cells with small driving forces for both hole and electron transfer," Adv. Mater. **30**(45), 1804215 (2018).
[7] J. Yan *et al.*, "Identifying structure–absorption relationships and predicting absorption strength of non-fullerene acceptors for organic photovoltaics," Energy Environ. Sci. **15**(7), 2958–2973 (2022).

[8]M. Riede, D. Spoltore, and K. Leo, "Organic solar cells—The path to commercial success," Adv. Energy Mater. **11**(1), 2002653 (2021).
[9]N. M. Kronenberg *et al.*, "Direct comparison of highly efficient solution- and vacuum-processed organic solar cells based on merocyanine dyes," Adv. Mater. **22**(37), 4193–4197 (2010).
[10]Z. Zhang and Y. Lin, "Organic semiconductors for vacuum-deposited planar heterojunction solar cells," ACS Omega **5**(39), 24994–24999 (2020).
[11]K. Cnops *et al.*, "8.4% efficient fullerene-free organic solar cells exploiting long-range exciton energy transfer," Nat. Commun. **5**(1), 3406 (2014).
[12]Q. Yue *et al.*, "Vacuum-deposited organic solar cells utilizing a low-bandgap non-fullerene acceptor," J. Mater. Chem. C **10**(7), 2569–2574 (2022).
[13]Y. Li *et al.*, "Simple non-fullerene electron acceptors with unfused core for organic solar cells," Chin. Chem. Lett. **30**(1), 222–224 (2019).
[14]P.I. Djurovich *et al.*, "Measurement of the lowest unoccupied molecular orbital energies of molecular organic semiconductors," Org. Electron. **10**(3) 515–520 (2009).
[15]J. Bertrandie *et al.*, "The energy level conundrum of organic semiconductors in solar cells," Adv. Mater. **34**(35), 2202575 (2022).
[16]W. Tress, K. Leo, and M. Riede, "Influence of hole-transport layers and donor materials on open-circuit voltage and shape of *I–V* curves of organic solar cells," Adv. Funct. Mater. **21**(11), 2140–2149 (2011).
[17]O. J. Sandberg, M. Nyman, and R. Österbacka, "Effect of contacts in organic bulk heterojunction solar cells," Phys. Rev. Appl. **1**(2), 024003 (2014).
[18]Q. Li *et al.*, "Insights into charge separation and transport in ternary polymer solar cells," ACS Appl. Mater. Interfaces **11**(3), 3299–3307 (2019).
[19]M. C. Scharber *et al.*, "Design rules for donors in bulk-heterojunction solar cells—Towards 10% energy-conversion efficiency," Adv. Mater. **18**(6), 789–794 (2006).
[20]D. C. Coffey *et al.*, "An optimal driving force for converting excitons into free carriers in excitonic solar cells," J. Phys. Chem. C **116**(16), 8916–8923 (2012).
[21]V. C. Nikolis *et al.*, "Field effect versus driving force: Charge generation in small-molecule organic solar cells," Adv. Energy Mater. **10**(47), 2002124 (2020).
[22]T. Zhang *et al.*, "Intrinsic measurements of exciton transport in photovoltaic cells," Nat. Commun. **10**(1), 1156 (2019).
[23]J. Wehner and B. Baumeier, "Multiscale simulations of singlet and triplet exciton dynamics in energetically disordered molecular systems based on many-body Green's functions theory," New J. Phys. **22**(3), 033033 (2020).
[24]U. Rau *et al.*, "Efficiency potential of photovoltaic materials and devices unveiled by detailed-balance analysis," Phys. Rev. Appl. **7**(4), 044016 (2017).
[25]A. Jungbluth, P. Kaienburg, and M. Riede, "Charge transfer state characterization and voltage losses of organic solar cells," J. Phys.: Mater. **5**(2), 024002 (2022).
[26]P. Kaienburg *et al.*, "Assessing the photovoltaic quality of vacuum-thermal evaporated organic semiconductor blends," Adv. Mater. **34**, 2107584 (2021).
[27]K. Ortstein *et al.*, "Band gap engineering in blended organic semiconductor films based on dielectric interactions," Nat. Mater. **20**(10), 1407–1413 (2021).
[28]Y. Dong *et al.*, "Orientation dependent molecular electrostatics drives efficient charge generation in homojunction organic solar cells," Nat. Commun. **11**(1), 4617 (2020).
[29]A. Baumann *et al.*, "A new approach for probing the mobility and lifetime of photogenerated charge carriers in organic solar cells under real operating conditions," Adv. Mater. **24**(32), 4381–4386 (2012).
[30]R. Meerheim, C. Körner, and K. Leo, "Highly efficient organic multi-junction solar cells with a thiophene based donor material," Appl. Phys. Lett. **105**(6), 063306 (2014).
[31]C. Koerner *et al.*, "Probing the effect of substrate heating during deposition of DCV4T:C60 blend layers for organic solar cells," Org. Electron. **13**(4), 623–631 (2012).
[32]V. Shrotriya *et al.*, "Accurate measurement and characterization of organic solar cells," Adv. Funct. Mater. **16**(15), 2016–2023 (2006).
[33]J. Lorrmann *et al.*, "Charge carrier extraction by linearly increasing voltage: Analytic framework and ambipolar transients," J. Appl. Phys. **108**(11), 113705 (2010).
[34]G. F. Burkhard, E. T. Hoke, and M. D. McGehee, "Accounting for interference, scattering, and electrode absorption to make accurate internal quantum efficiency measurements in organic and other Thin solar cells," Adv. Mater. **22**(30), 3293–3297 (2010).
[35]W. Shockley and H. J. Queisser, "Detailed balance limit of efficiency of *p-n* junction solar cells," J. Appl. Phys. **32**(3), 510–519 (1961).
[36]U. Rau, "Reciprocity relation between photovoltaic quantum efficiency and electroluminescent emission of solar cells," Phys. Rev. B **76**(8), 085303 (2007).
[37]K. Vandewal *et al.*, "On the origin of the open-circuit voltage of polymer–fullerene solar cells," Nat. Mater. **8**(11), 904–909 (2009).